https://dx.doi.org/10.1016/j.envpol.2019.01.047

Concurrent Adsorption and Micro-electrolysis of Cr(VI) by Nanoscale Zerovalent Iron/Biochar/Ca-Alginate Composite

Zhonghao Wan[1], Dong-Wan Cho[1], Daniel C.W. Tsang[1,*], Meng Li[2], Tan Sun[3], Francis Verpoort[4,5]

[1] Department of Civil and Environmental Engineering, The Hong Kong Polytechnic University, Hong Kong

[2] School of Civil Engineering & Architecture, Wuhan University of Technology, P.R. China

[3] College of Environmental Science and Engineering, Tongji University, P.R. China

[4] Laboratory of Organometallics, Catalysis and Ordered Materials, State Key Laboratory of Advanced Technology for Materials Synthesis and Processing, Wuhan University of Technology, P.R. China

[5] Department of Inorganic and Physical Chemistry, Ghent University, Krijgslaan 281-S3, 9000 Ghent, Belgium

[*] Corresponding author: dan.tsang@polyu.edu.hk

Abstract:

This study introduced a new approach for simultaneously enhancing Cr(VI) removal performance and mitigating release of dissolved Fe during nanoscale zero-valent iron (nZVI)-mediated reactions. After entrapping nZVI-impregnated biochar (BC) in the matrix of calcium-alginate (CA) bead, the physicochemical characterizations of nZVI/BC/CA composites revealed that nZVI/BC particles were embedded inside CA having a spherical shape and several cracks on its outer layer. The multi-functionality of nZVI/BC/CA composites consisting of reductant (nZVI), porous adsorbent (BC), and external screening layer (CA) enhanced the removal of Cr(VI) with maximum adsorption capacity of 86.43 mg g^{-1} (based on the Langmuir isotherm) and little release of dissolved Fe. With the XPS analysis and fitting results of kinetics (pseudo second order) and isotherms (Redlich-Peterson model), plausible removal mechanisms

of Cr(VI) were simultaneous adsorption and micro-electrolysis reactions by nZVI/BC/CA composites. The practical applicability of nZVI/BC/CA composites was demonstrated through the fixed-bed column experiments. These results provide new insights into the design of high-performance engineered biochar for wastewater treatment.

Keywords: engineered biochar; metal-biochar composite; solid-supported nZVI; hexavalent chromium; adsorption-reduction.

1. Introduction

As one of the most typical potentially toxic elements, chromium (Cr) poses serious threat to the environment and human health due to its high toxicity, carcinogenicity, environmental persistence, and bioaccumulation in food chain (Cheng et al., 2010; Sazakli et al., 2014). Proper treatment of concentrated Cr-containing wastewater generated from the stainless steel, electroplating, and dyeing industries has become a global issue. The species of Cr(VI) such as chromate ($HCrO_4^-$, CrO_4^{2-}) and dichromate ($Cr_2O_7^{2-}$) are mobile and toxic in natural environment, while Cr(III) is relatively stable, insoluble, and easy to precipitate (Jobby et al., 2018). Thus, the conversion from Cr(VI) to Cr(III) ion (Cr^{3+}) could be an effective way to reduce the risk of chromium contamination (Wan et al., 2018).

Various adsorption processes have been designed and studied with the development of efficient adsorbents due to the outstanding potential in the soil remediation/wastewater treatment during the past decades. Among the adsorbents, engineered biochar has showed the great effectiveness for the soil remediation by inducing changes in favourable geochemical conditions and effectively immobilizing metals/metalloids (Ahmad et al., 2017; Beiyuan et al.,

2017; Fang et al., 2016). The soil quality has been remarkably improved with the redox changes in the soil environment and the reduction in the mobility of oxyanions by the addition of biochar (Beiyuan et al., 2017; Feng et al., 2018). Beside the use for soil stabilization, engineered biochar has been also used as adsorbent for the elimination of heavy metal from wastewater and its adsorption function has been demonstrated (Cho et al., 2017a; Cho et al., 2017b).

Given that the validated way to control the chromium contamination is reduction of Cr(VI) to Cr(III) as aforementioned above (Liu et al., 2008; Shevchenko et al., 2008), Biochar or magnetite-containing biochar mediated Cr(VI) reduction can be a good option since good efficiency of them has been proven in a broad range of pH. However, the important issue that the deposition of reactive materials onto biochar needs to be improved for better removal of Cr(VI) still remains because of the technical limitation including the weak reducing potentials of biochar itself and magnetite (Rajapaksha et al., 2018; Zhong et al., 2018).

Meanwhile, zero-valent iron (Fe) has been regarded as an efficient reductant for the removal of organic and inorganic pollutants (Mortazavian et al., 2018; Ren et al., 2018; Sun et al., 2017). Compared with other metal reductants such as Zn and Mn, Fe possesses several advantages of easy availability, nontoxicity and cost-effectiveness, which makes it more applicable in the water treatment (Lv et al., 2018). In particular, nanoscale zero-valence iron (nZVI) showed great prospect in environmental remediation due to its high reactivity and multifunctionality. Therefore, nZVI was chosen as a main reactive material in this work. However, the application of nZVI was restricted by its strong conglomeration and instability (Ahmed et al., 2017), and the potential transformation and ecological effects of Fe nanoparticles have been addressed (Lei et al., 2018b). To overcome these weaknesses, the

introduction of carrier to immobilize nZVI is considered as the ideal solution to enhance the stability of nZVI (Lei et al., 2018a). Entrapping nZVI particles in polymeric matrix has been effective but not sufficiently durable (Lei et al., 2018a; Sun et al., 2018). On the other hands, biochar-nZVI composites exhibited high distribution of nanoparticles on the surface and simultaneoulsy enhanced the reactivity and stability owing to the porous structure and oxygen-containing functional groups of biochar (Feng et al., 2018; Rajapaksha et al., 2018; Vikrant et al., 2018; Yang et al., 2018) . Despite the advantages of using biochar as a support, the Fe leaching during the redox reaction can cause secondary contamination to the aquatic environment, which may hinder the application feasibility of composites. Thus, another layer that can screen the release of dissolved Fe ions to the environment is needed to design the environmentally benign biochar-nZVI system.

Calcium alginate (CA) bead is a good candidate of external protector for biochar-nZVI composites to reduce the adverse effects because alginate contains abundant functional groups that can efficiently uptake the dissolved metal ions (Banerjee et al., 2018; Wang, B. et al., 2018). To the best of our knowledge, the effort to increase the applicability of the composites with the entrapment by CA has not been made yet. Due to the large fraction of aromatic carbon (high ratios of C/H and C/O) of wheat bran, it was selected as biochar precursor to provide the well-structured porous structure for highly distribution of nZVI. Thus, we first fabricated the novel composites consisting of nZVI, biochar, and CA, and investigated the feasibility of using the resulting composites to remove Cr(VI) in aqueous solution without a large loss of reactivity and Fe leaching. The main objectives of this study are to: (a) develop an effective, low-cost and eco-friendly biochar-nZVI composite using CA ; (b) evaluate and compare the Cr(VI)

adsorption performance of yielded nZVI impregnated biochar composite entrapped in CA (nZVI/BC/CA), calcium alginate (CA) and nZVI impregnated biochar (nZVI/BC) by analyzing the effect of pH, adsorption kinetics, adsorption isotherms and intraparticle model fitting; (c) characterize the yielded composite thoroughly (e.g. SEM, EDS, FTIR, Raman, XPS, etc.) and investigate the adsorption mechanism within; (d) test the adsorption capability and longevity of yielded composite using the fixed-bed column experiments.

2. Materials and Methods

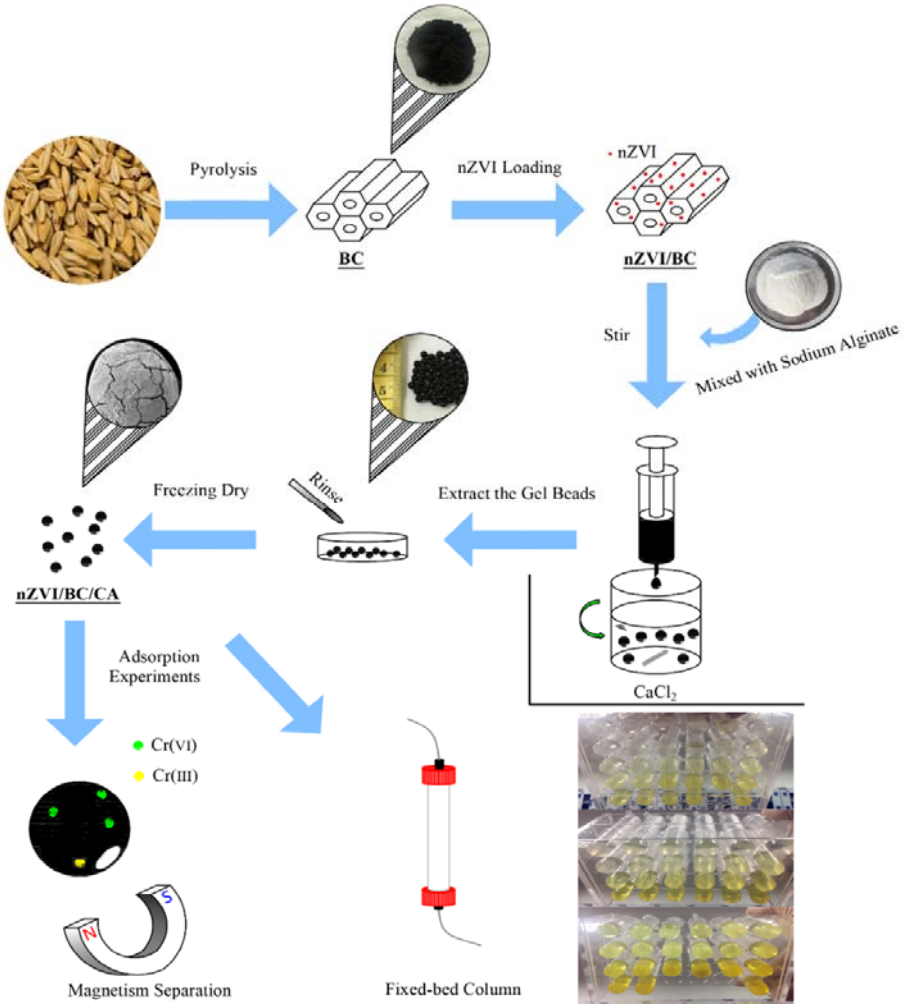

Fig. 1. Schematic diagram of production and adsorption process.

2.1 Reagents and implements

Wheat bran provided from Tongji University was chosen as the feedstock biomass. Sodium alginate and calcium chloride were purchased from Sigma–Aldrich Co., Ltd without further purification. Potassium chromate (K_2CrO_4) dissolved in deionized water for preparing hexavalent chromium solutions was obtained from the Sinopharm Chemical Reagent Co., Ltd. All basic reagents were analytical grade, and purchased from Sinopharm Chemical Reagent Co., Ltd. All containers (e.g. flasks, beaker, and mass cylinder) in adsorption experiments were made of plastic materials.

2.2 Preparation of nZVI/BC/CA Composite

The nZVI/BC were prepared following a modified method (Wu et al., 2018): Derived wheat bran was oven dried (80°C) and grounded into powder. Then the raw biomass powder was pyrolyzed at 500 °C for 3 hours with a heating rate of 15 °C min^{-1} in muffle furnace at an inert atmosphere (N_2). The collected biochar was rinsed with deionized water to remove ash component and dried for 8 h. The dried biochar was grounded to pass a 0.25 mm bore diameter sieve and stored in sealed desiccator. In addition, $FeCl_3 \cdot 6H_2O$ (4.41 g) were dissolved in 100 mL deionized water and the pH of solution was adjusted with dilute 0.1 M NaOH and 0.1 M HNO_3 to 5.0. Then, 1.0 g of yielded biochar was added to solution and agitated at 160 rpm and 25 °C for 1 h. Subsequently, 0.05 M $NaBH_4$ was added dropwise by syringe under inert atmosphere (N_2) till the molar mass ratio of $FeCl_3 \cdot 6H_2O$ and $NaBH_4$ reached 4:3 in order to form nZVI. After that, the solution was vigorously stirred at 500 rpm in 25 °C water bath for 30 min. During this process, nZVI was impregnated on the surface of BC and the mass ratio of

121 nZVI and BC was 1:1. The nZVI/BC were obtained by centrifugation under 2000 rpm and
122 rinsed with alcohol and deoxygenated water for three times. The collected nZVI/BC were
123 transferred in freeze dryer for 5 h and then stored in sealed desiccator.

124 Preparation of nZVI/BC/CA composite followed a modified liquid-phase method (Wang,
125 Bing et al., 2018): Sodium alginate was dissolved in deionized water (1% w/v) and the yielded
126 nZVI/BC was added slowly into the solution till the mass ratio of nZVI/BC and alginate
127 reached 4:1. Ultrasonic Cleaner was applied to avoid the conglomeration of nZVI/BC. Then
128 the 50 mL mixture of nZVI/BC and sodium alginate was added dropwise into 200 mL 0.1 M
129 $CaCl_2$ solution (contained 5 mL ethyl acetate) by syringe to form nZVI/BC/CA beads. Then
130 slowly agitating for 3 h under 25°C to solidify the gel beads, the residual solution was removed
131 and the yielded gel beads were collected. The gel beads were rinsed with deionized water for
132 three times and stored in sealed container. Besides, pure Ca-alginate beads were prepared as a
133 control for characterization by similar process without the addition of nZVI/BC.

134 2.3 Characterizations

135 The functional groups of nZVI/BC/CA composite were measured by FTIR (Nicolet 6700
136 spectrometer, USA) and Raman spectrum shift measurements (Renishaw Raman spectrometer,
137 UK). The morphology and element point scanning were characterized by SEM (JSM-IT300,
138 Japan) and EDS (JXA-8230, Japan). The XRD patterns were obtained (D8 Advance
139 diffractometer, Germany) to identify the crystalline information of composites. The surface
140 elements of the biochar were characterized with XPS (ESCALAB 250Xi spectrometer, USA).
141 TG (Discovery TGA, USA) was performed under air atmosphere at a heating rate of 20 °C min

142 $^{-1}$. The BET analysis (TriStar-II 3020, USA) was obtained to investigate the pore volume. All
143 tests were conducted in triplicates.

144 2.4 Batch Adsorption Experiments

145 The adsorption performance of nZVI/BC/CA composite was assessed in batch adsorption
146 experiments at 25°C in triplicates. The pH of Cr(VI) solutions was adjusted with dilute NaOH
147 (0.1 M) and HNO_3 (0.1 M). 1 g/L of nZVI/BC/CA composite was added to Cr(VI) solution
148 with a specific concentration (150mg/L if not specify) in a flask. Then the mixed solution was
149 put in a thermostatic shaker at 160 rpm for 24 h. After that, the Cr(VI) and Cr(III) concentration
150 of the supernatant were measured and the adsorbents were washed with deionized water and
151 collected for followed characterization. The concentration of Cr(VI) in the supernatant was
152 measured using a UV spectrophotometer (UV-1100, China) at a maximum wavelength of 540
153 nm after complexation with 1,5-diphenylcarbazide (Chen et al., 2011). The leakage of Fe was
154 measured by inductively coupled plasma-optical emission spectrometry (Prodigy 7, USA) and
155 the mass ratio of nZVI/BC and nZVI/BC/CA addition in pH batch experiments was 1:3
156 according to the TG analysis. For the quantification of Cr(III), the Cr(III) was oxidized to Cr(VI)
157 by potassium permanganate at 100°C for 3h and then measured. The isotherm experiments
158 were conducted by varying the initial Cr(VI) concentrations with a range of 10−1000 mg/L and
159 the kinetics experiments were carried out by varying the reaction time. The effect of initial
160 solution pH on Cr(VI) removal was determined by varying the pH of solution with dilute NaOH
161 and HNO_3 under initial Cr(VI) concentration.

2.5 Adsorption kinetic and isotherm modeling

Three kinds of kinetic modeling including Pseudo first-order, Pseudo second-order and Elovich were carried out in this paper, which are expressed by the equation (1), (2) and (3), respectively (Lecca, 2013).

$$\ln(q_e - q_t) = \ln q_e - k_1 t \tag{1}$$

where q_t and q_e are the amounts of solute adsorbed at time t and at equilibrium per unit weight of adsorbent (mg g^{-1}), respectively; k_1 (min^{-1}) is the rate constant of pseudo first-order.

$$\frac{t}{q_t} = \frac{1}{k_2 q_e^2} + \frac{t}{q_e} \tag{2}$$

where q_t and q_e are the amounts of solute adsorbed at time t and at equilibrium per unit weight of adsorbent (mg g^{-1}), respectively; k_2 (min^{-1}) is the rate constant of pseudo second-order and h (mg g^{-1} min^{-1}) is the initial adsorption rate.

$$\frac{C_t}{C_0} = 1 - \frac{m}{\beta V C_0} \ln(1 + \alpha\beta t) \tag{3}$$

where C_0 and C_t are the concentration of solute at initial time and time t (mg L^{-1}), respectively; V (L) is the volume and m (mg) is amount of adsorbent; α and β are the rate constant of Elovich.

Three kinds of isotherm modeling including Langmuir, Freundlich and Redlich-Peterson were carried out in this paper (Foo and Hameed, 2010), which are expressed by the equation (4), (5) and (6), respectively.

$$q_e = K_F C_e^{\frac{1}{n}} \tag{4}$$

Where C_e (mg L^{-1}) is the aqueous phase equilibrium concentration in the supernatant; q_e (mg g^{-1}) is the amount of adsorbate adsorbed per unit weight; K_F (L mg^{-1}) is the Freundlich constant related to the rate of adsorption.

$$q_e = \frac{q_m K_L C_e}{1 + K_L C_e} \tag{5}$$

Where C_e (mg L^{-1}) is the aqueous phase equilibrium concentration in supernatant; q_e (mg g^{-1}) is the amount of adsorbate adsorbed per unit weight; q_m (mg g^{-1}) and K_L (L mg^{-1}) are the Langmuir constants related to adsorption capacity and the rate of adsorption, respectively.

188 $$q_e = \frac{KC_e}{1+\alpha C_e^{\beta}} \quad (6)$$

189 Where C_e (mg L^{-1}) is the aqueous phase equilibrium concentration in supernatant; q_e (mg
190 g^{-1}) is the amount of adsorbate adsorbed per unit weight; K and α are the Redlich−Peterson
191 isotherm constants and β is the exponent, which ranges between 1 and 0.

192 The intraparticle diffusion model (5) by Weber and Morris(Wang et al., 2015) was used to
193 analyze the surface adsorption reaction. The equation can be represented as follows.

194 $$q_t = k_i t^{\frac{1}{2}} + c \quad (7)$$

195 where q_t (mg g^{-1}) is the amount of adsorbate adsorbed per unit weight at time t; C is the
196 intercept (mg g^{-1}) and k_i is the intraparticle diffusion rate constant (mg g^{-1} min^{-1}) of adsorption
197 step.

198 2.6 Fixed-bed column experiments

199 Circular reactor with 2 cm of inner diameter and 10 cm of height was applied as fixed-
200 bed column in the fixed-bed column experiments. 10g nZVI/BC/CA composite was fixed in
201 the bottom of column by two pieces of hydrophilic sieve plates (50 μm bore diameter) and
202 forming a biochar layer with 5cm height. The initial Cr(VI) concentrations of C_0 were 150, 200
203 and 250 mg/L. In different experiments, solutions with different initial Cr(VI) concentrations
204 (150, 200 and 250 mg/L) passed through the column with a specific flow rate (0.5 mL/min)
205 using a peristaltic pump. All column experiments were conducted at 25±1°C in triplicates. To
206 maintain the solution pH=4, 1 mM phosphate buffer was added into the reaction solution. The
207 background solutions contained 1 mM $CaCl_2$ and 1 mM $NaNO_3$ to maintain a constant ionic
208 strength (Peng et al., 2017; Zhu et al., 2018). The Cr(VI) concentrations of effluent was

measured with a specific interval from the outlet. The breakthrough curves were fitted by Thomas model. The equation can be represented as follows (Volesky, 2007):

$$\frac{C_e}{C_0} = \frac{1}{1+\exp(\frac{K_{TH}q_m x}{v} - K_{TH}C_0 t)} \quad (8)$$

Where k_{TH} (mL / min·mg) was the Thomas constant; q_m related to adsorption capacity; v (mL/min) was the velocity of flow; x (g) was the weight of the beads; t (min) was the breakthrough time.

3. Results and Discussion

3.1 Characterization of composites

The SEM results of BC, nZVI/BC, CA and nZVI/BC/CA were depicted in the Fig. S1. Compare to the flake morphology of BC (Fig. S1A), Fig. S1B revealed that nZVI/BC showed a different surface morphology as rough char material with irregular particles on its surface, attributed to the impregnation of nZVI on BC. The overall size of nZVI/BC composites turned relatively smaller because they were crushed during stirring and centrifugation processes in production and this might expose more inner pore structures of BC, which was beneficial to the impregnation process. The typical images of CA and nZVI/BC/CA were shown in Fig. S1C and Fig. S1D, respectively. Fig. S1D indicated that nZVI/BC/CA possessed relatively rough surface morphology with irregular stretch, which was made by the addition of nZVI/BC.

The elemental composition and the surface structure of BC, nZVI/BC, CA and nZVI/BC/CA were also analyzed by SEM/EDS and the results are presented in Fig. 2. The SEM images of BC and nZVI/BC exhibited a common porous structure of biochar (Fig. 2A)

230 and the deposition of particles on the surface of BC and the blockage of pore structure caused
231 by particles were observed in nZVI/BC (Fig. 2B). The observed particles on the surface of
232 nZVI/BC consisted of Fe element (29.66%), confirming the formation of nZVI. Similarly, it
233 was also confirmed that nZVI/BC was successfully entrapped in the CA beads when
234 considering the detected Fe element in spectrum 4 and 5 (EDS data of nZVI/BC/CA). By the
235 comparison between CA (Fig. 2C) and nZVI/BC/CA (Fig. 2D), an outer layer with a clear
236 dividing line could be found on the outmost part of nZVI/BC/CA composite. Based on the EDS
237 data of the outside and inside nZVI/BC/CA it was revealed that the outer layer of CA contained
238 less weight percentage of Fe element (7.6 wt.%) than that detected in its inner structure (18.34
239 wt.%). This interesting observation might be due to the polarity and hydrophilicity of alginate,
240 which led to the conglomeration of alginate molecules on the surface in the formation process
241 of gel beads. The decrease in the weight percentage of Fe element (from 29.66 wt.% to 18.34
242 wt.%) by CA introduction indicates nZVI/BC was mainly embedded inside CA.

243 The crystalline structures of the composites were characterized by X-Ray diffraction and
244 the patterns were illustrated in Fig. 3A. The pattern of nZVI sample showed the main peak at
245 44.7° assigned to nZVI and the peaks at 31.76°, 45.52°, 57.08° and 62.72° assigned to iron
246 oxide (Fe_3O_4) (Dong et al., 2017b), which is a typical core-shell structure of nZVI. The patterns
247 of BC and nZVI/BC indicated that the nZVI was successfully impregnated on the surface of
248 BC. The decreased diffraction peak at 44.7°of nZVI/BC/CA might come from the increase of
249 intermolecular spacing and amorphousness after the entrapment in CA (Yen et al., 2011). Due
250 to the existence of Fe_3O_4, nZVI/BC/CA possessed favorable magnetism for separation after
251 batch experiments.

252 FTIR was applied to examine functional groups of BC, nZVI/BC, nZVI/BC/CA and
253 nZVI/BC/CA after adsorption. As shown in Fig. 3B, for BC there were five major peaks at
254 ~3433, ~1683, ~1345, ~1045 and ~632 cm^{-1} corresponding to the stretching vibration of -OH,
255 C=O, -COOH and C-H, respectively (Ahmed et al., 2016). After the impregnation of nZVI, the
256 peaks at ~3440, ~1345 and ~632 cm^{-1} significantly decreased, suggesting the bonding of nZVI
257 with -OH. The peaks at ~3412, ~1683 and ~1045 cm^{-1} slightly increased after the entrapment
258 of nZVI/BC in CA, which indicated that the addition of CA enriched the quantity of functional
259 groups (Periyasamy et al., 2018). The fact that the main functional groups of nZVI/BC/CA
260 notably decreased after adsorption experiments confirmed that there were chemical reactions
261 between nZVI/BC/CA and Cr species.

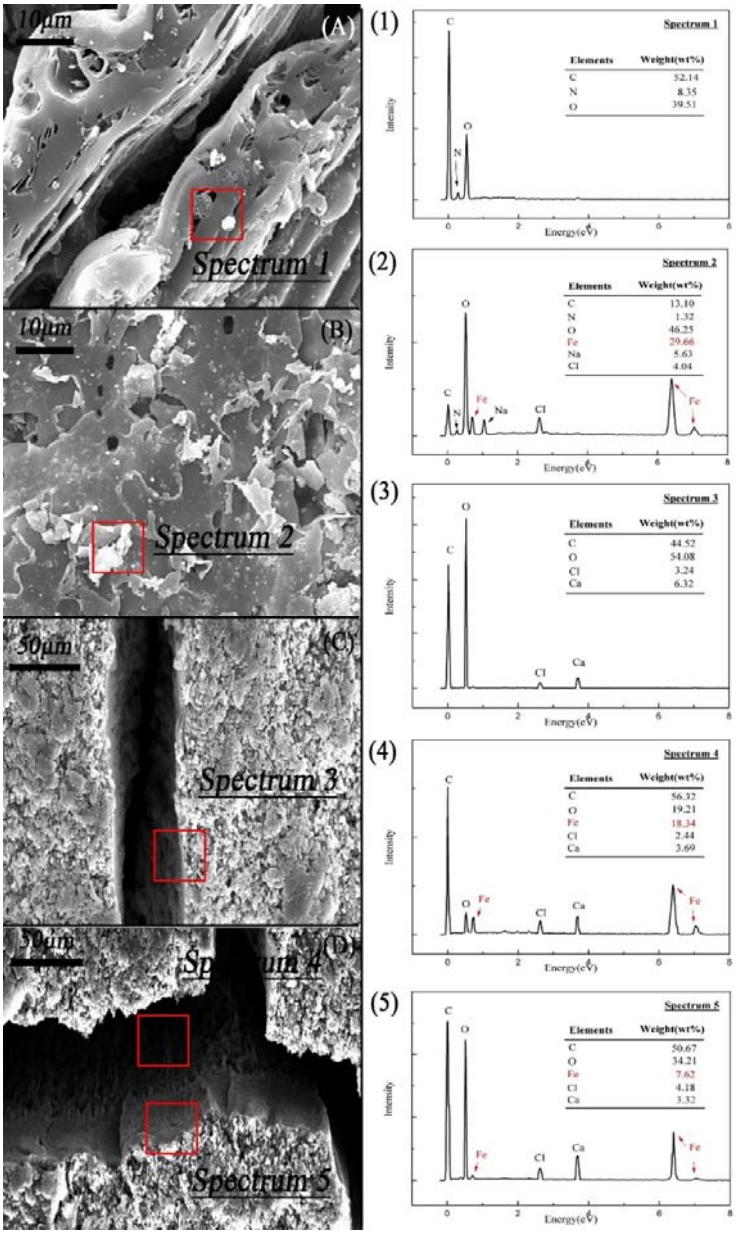

Fig. 2. SEM-EDS of BC, nZVI/BC, CA and nZVI/BC/CA.

The Raman spectroscopy was applied to investigate the phases of iron oxides and the graphitization/functionalization of nZVI/BC and nZVI/BC/CA. As shown in Fig. 3C, nZVI sample showed peaks at 223, 292, 486 and 1320 cm^{-1} which were credited to bands of the well-established hematite (α-Fe_2O_3) and the peak at 682 cm^{-1} was assigned to magnetite (Fe_3O_4) (Dong et al., 2017b). The existence of iron oxides coincided with the XRD analysis. The peak

at ~398 cm^{-1} corresponded to α-FeOOH and γ-FeOOH. After impregnation of nZVI, nZVI/BC showed same peaks at 223, 292, ~398, ~486 and ~682 cm^{-1} which indicated the presence of magnetite Fe_3O_4 (i.e., imparting magnetism property of nZVI/BC) and confirmed the consumption of -OH during the formation of FeOOH. This conclusion of nZVI/BC/CA coincided with that of nZVI/BC. Raman spectrum of BC showed two main peaks at ~1372 and ~1590 cm^{-1}, which were assigned to the sp^3 carbon atoms of disordered graphite (D band) and the sp^2 carbon atoms of in-plane vibration (G band). The ratio of disordered graphite (D band) intensity and in-plane vibration (G band) intensity, namely I_D/I_G, indicated the graphitization degree and the functionalization degree of biochar. It could be found that I_D/I_G values of nZVI/BC, nZVI/BC/CA and nZVI/BC/CA after adsorption decreased with the increasing consumed amount of functional groups. The results above corresponded to that of FTIR analysis.

Fig. 3D provided the TG analysis of nZVI/BC/CA composite. Specifically, the mass decay below 200 °C was attributed to the evaporation of adsorbed water. The mass decay between 200 and 500 °C was due to the degradation of the main chains of alginate, indicating that the entrapped nZVI/BC could account for more than 30% mass ratio of the composite. According to DTG curve, the degradation of the composite was non-spontaneous exothermic reaction near 300 and 420 °C.

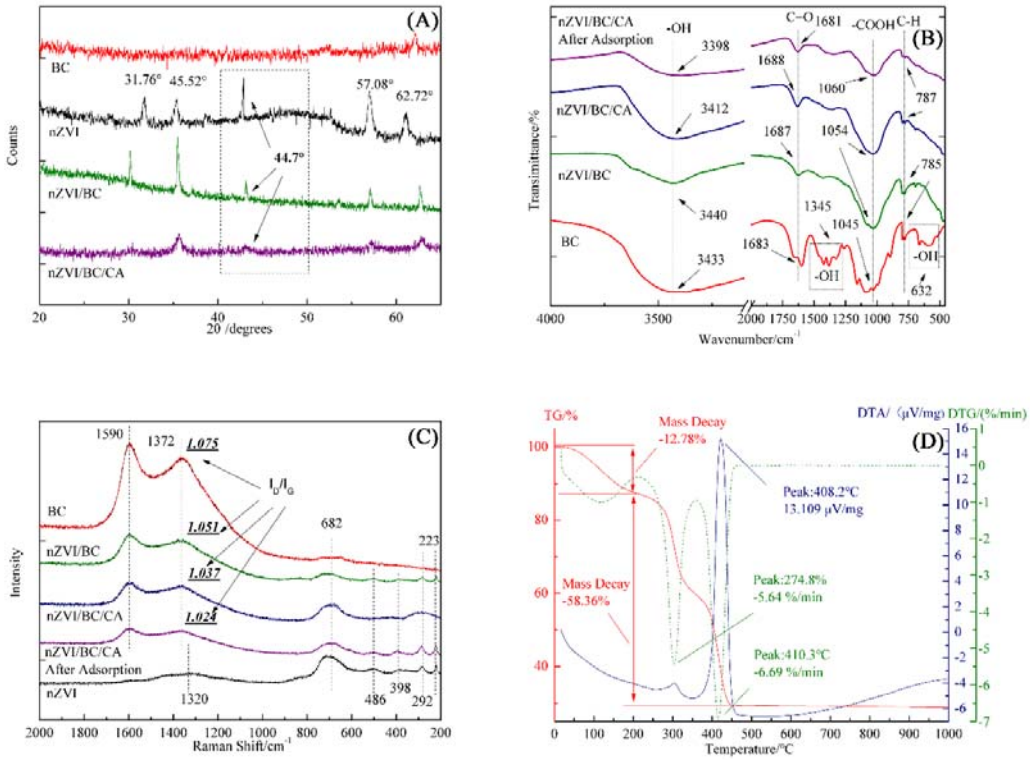

Fig. 3. (a) XRD patterns of BC, nZVI, nZVI/BC and nZVI/BC/CA; (b) FTIR spectrums of BC, nZVI/BC, nZVI/BC/CA and nZVI/BC/CA after adsorption; (c) Raman spectrums of BC, nZVI, nZVI/BC, nZVI/BC/CA and nZVI/BC/CA after adsorption; and (d) TG analysis of nZVI/BC/CA.

3.2 Cr adsorption

The yielded BC, CA, nZVI/BC and nZVI/BC/CA were used for the batch adsorption experiments. As shown in Fig. 4A, the Cr(VI) removal performance of nZVI/BC was stable and continued to decrease slightly with the increase of pH. In addition, the Cr(VI) adsorption capacity of CA was notably affected and declined to below 10 mg/g due to the deprotonation of functional groups and the change of Cr(VI) speciation from $Cr_2O_7^{2-}$ to CrO_4^{2-}. The Cr(VI) adsorption capacity of nZVI/BC/CA was similar to the sum of those of nZVI/BC and CA. The

299 results indicated that the functional groups of CA were more sensitive to pH and Cr speciation
300 change than nZVI/BC, probably because the Cr(VI) removal by nZVI/BC was mainly
301 attributed to the reduction of Cr(VI) by nZVI. The pH change of nZVI/BC/CA between the
302 initial pH and the final pH was depicted in Fig. S6. The solution pH was slightly increased,
303 which could result from the depletion of H^+ by interactions on nZVI/BC/CA surface. Besides,
304 the Fe leakage (due to the dissociation of nZVI/BC and redox reaction with Cr(VI)) from the
305 suspensions of nZVI/BC and nZVI/BC/CA was also depicted in Fig. 4A. The reduction reaction
306 of Cr(VI) could proceed actively under the acidic condition since a number of hydrogen ions
307 needed for the reduction are provided, which was supported by the increased release of Fe ions
308 with the decreasing solution pH. The introduction of CA notably decreased the concentration
309 of dissolved Fe ions, which can be explained by ion exchange of Fe with Ca ions present in the
310 gel beads (Jung et al., 2015). In addition, the uptake of Cr(VI) by outer layers (CA) was also
311 enhanced due to the complexation with exchanged Fe ions inside the matrix. These
312 observations suggest that the entrapment of CA increased the Cr(VI) removal performance and
313 reduced the release of Fe ions to the environment. The optimal pH condition for the best
314 removal of Cr(VI) was pH=4 in nZVI/BC/CA system. Furthermore, the developed composite
315 (nZVI/BC/CA) is proposed to be applied to the treatment of acidic wastewater contaminated
316 by Cr(VI) because there is no concern about the sharp increase of dissolved Fe ions with the
317 use of the composites.

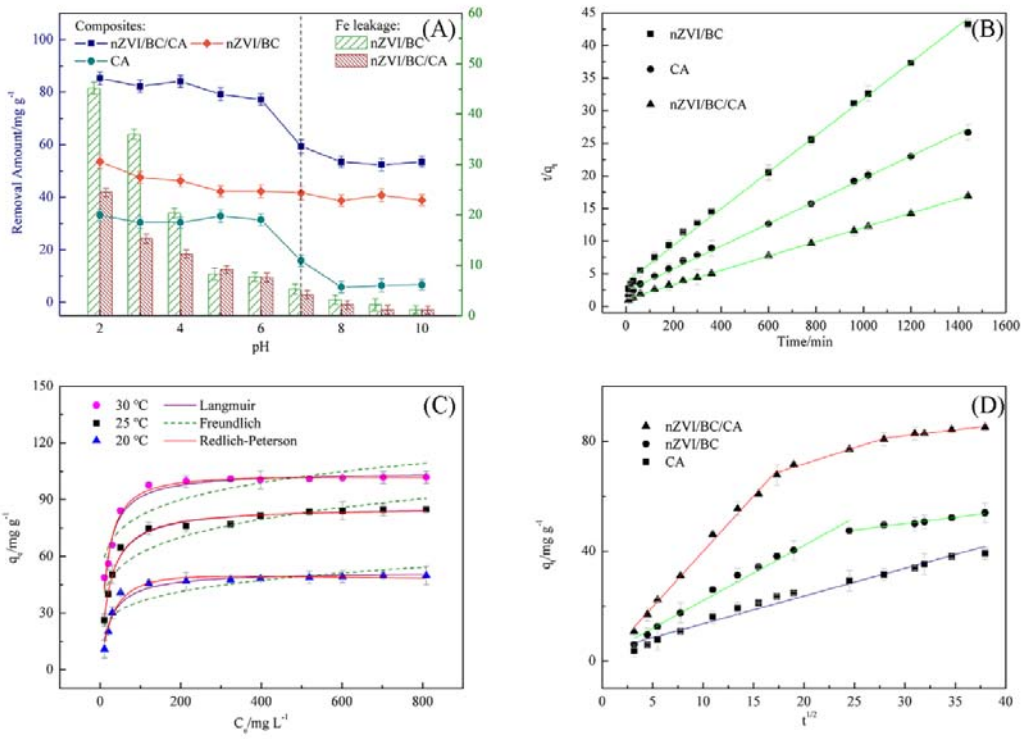

Fig. 4. (a) The effect of initial solution pH on Cr(VI) removal and Fe leakage; (b) Pseudo second order fitting of nZVI/BC, CA and nZVI/BC/CA (contact time = 24 h, temperature = 25°C, pH=4); (c) Isotherm fitting of nZVI/BC/CA under different reaction temperature (contact time = 24 h, temperature = 25°C, pH=4); and (d) Intraparticle diffusion model fitting of nZVI/BC, CA and nZVI/BC/CA (contact time = 24 h, temperature = 25°C, pH=4).

The kinetics data of Cr(VI) removal were shown in Table S1,S2 and S3 with C_0 of 150 mg/L. The pseudo first order model, the pseudo second order model and the Elovich model were employed to analyze the adsorption process and the curves were shown in Fig. S2, Fig. 4B and Fig, S3. The pseudo first order model (PFO) applied to physical adsorption and the pseudo second order (PSO) model was applicable to the materials with finite adsorption capability (both chemical and physical adsorption) while the Elovich model was suitable to the materials with heterogeneous surface (chemical adsorption). The fittings by three kinetic

models achieved the high level of correlation coefficients (R^2) (0.949-0.989 for PFO, 0.997-0.999 for PSO and 0.974-0.994 for Elovich), respectively, suggesting that both physical and chemical reaction on the surface are main adsorption mechanisms. The fitting results support that the main removal mechanisms are closely associated with the physical adsorption by porous structure (*i.e.*, BC and CA) and the chemical adsorption by the large number of functional groups (*i.e.*, CA) and reduction sites (*i.e.*, nZVI) in the composite detected by the characterizations.

The Cr(VI) adsorption isotherms of nZVI/BC/CA at 20, 25 and 30 °C were shown in Fig. 4C. Three typical isotherm models (Langmuir, Freundlich and Redlich-Peterson) were chosen to fit the Cr(VI) adsorption data of nZVI/BC/CA. The Cr(VI) adsorption capacity of nZVI/BC/CA increased gradually with the increase of temperature, which was due to the fact that the rise of temperature increased the contact chance among solution ions and functional groups, indicating that the reaction was an endothermic adsorption process. As shown in Table S4, Langmuir was the more suitable isotherm model than Freundlich. Langmuir was suitable for monolayer adsorption while Freundlich model could be applied to both monolayer or multilayer adsorption and the favorable R^2 value of Langmuir suggested that the outer layer dominated in the adsorption process. Redlich-Peterson was applicable to hybrid adsorption (both chemical and physical adsorption) and provided optimal fitting results in Table S5, which coincided with the conclusion in the kinetics. The maximum Cr(VI) adsorption capacity of nZVI/BC/CA can be obtained by Langmuir model and it was 86.43 mg/g (25°C, pH=4). The maximal Cr(VI) adsorption capacity of nZVI/BC/CA was better than many related materials reported in the literature (Table 1).

353

354 Table 1. Cr(VI) removal efficiency by related materials

Items	Optimal pH	Maximum adsorption capacity (mg/g)	References
nZVI/BC/CA	4	86.43	This work
CA	5	33.24	This work
Ferric ion-laden char	6	53.45	(Li et al., 2010)
rGO-nZVI	2.9	50.1	(Ren et al., 2018)
Fe3O4@n-HApAlg	4.2	29.14	(Periyasamy et al., 2018)
nZVI@HCl-BC	5	18.8	(Dong et al., 2017a)
Bio-functional Magnetic Beads	1	6.73	(Li et al., 2008)
AC/nZVI	4	4.80	(Mortazavian et al., 2018)

355 The intraparticle diffusion model, the linear fitting of q_t and $t^{1/2}$, was applied to analyze
356 the adsorption reaction stages of CA, nZVI/BC and nZVI/BC/CA. If the extended lines of
357 curves passed through origin point, then the intraparticle diffusion (physical adsorption) took
358 the dominant effect of adsorption process. As shown in Fig. 4D, the first stage of CA, nZVI/BC
359 and nZVI/BC/CA curves all pointed to the origin point, suggesting the initial adsorption was
360 led by the intraparticle diffusion. Two other stages in the curve of nZVI/BC/CA and one extra
361 stage in the curve of nZVI/BC could be involved with chemical adsorption and redox reaction.
362 Specifically, chemical adsorption or redox reaction gradually dominated with the intraparticle
363 diffusion of Cr(VI) to the inner micropores of materials, which led to the change of curve slope.
364 Compared with nZVI/BC, nZVI/BC/CA possessed higher adsorption capacity and more
365 complex structure, which resulted in one extra stage of curve. In addition, the slopes of
366 nZVI/BC/CA curve were always higher than nZVI/BC and CA curves, suggesting the removal
367 efficiency of nZVI/BC/CA.

368 3.3 Cr removal mechanism

369 Combined with the conclusions in characterization and batch experiments, it could be
370 confirmed that the Cr(VI) removal by nZVI/BC/CA resulted from both physical processes (e.g.
371 physical adsorption) and chemical processes (e.g. chemical adsorption, redox reaction, etc.).
372 To obtain a better understanding of the mechanism within the interaction between nZVI/BC/CA
373 and Cr species, XPS was adopted to investigate the elemental compositions of composites and
374 Fe oxidation states before and after the uptake of Cr species.

375 As shown in Fig. 5A, the survey indicated the elemental changes of nZVI/BC/CA and a
376 typical Cr peak appeared after adsorption due to the uptake of Cr species in nZVI/BC/CA
377 sample. After deconvoluting and fitting, five major peaks of Fe 2p were depicted in Fig. 5B
378 and 5C. Specifically, FeOOH, Fe(III), FeOOH, Fe_2O_3, and FeO corresponded to the peaks at
379 723.4, 717.7, 711.6, 710.1 and 708.9, respectively(Lyu et al., 2017). The intensity of Fe species
380 peaks significantly increased after adsorption, suggesting nZVI was oxidized to iron oxides
381 during the uptake of Cr species which confirmed the formation of nZVI. In addition, the
382 percentage ratios of FeOOH (51.9% to 54.5%) and Fe(III) (4.9% to 12.7%) increased while
383 those of FeO (18.8% to12.7%) and Fe_2O_3 (24.4% to 20.2%) decreased, indicating that a part
384 of Fe(II) species was oxidized to Fe(III) species. Fig. 5D indicated the concurrent presence of
385 Cr(VI) and Cr(III), confirming the participation of redox reaction in Cr(VI) removal. The
386 typical Cr 2p XPS peaks were assigned at 579.2 eV for Cr(VI) and 577.2 eV for Cr(III) (Ma et
387 al., 2014) and the percentage ratios of Cr(VI) and Cr(III) species were 34.3% and 65.7%,
388 respectively. The results above indicated that Cr(VI) was reduced to Cr(III) by the reduced Fe
389 species [Fe(II) or Fe(0)] entrapped in CA and nZVI/BC/CA showed a good adsorption

performance in removal of both Cr(VI) and Cr(III) species.

To further investigate the Cr(VI) reduction capability of nZVI/BC/CA, the amount of Cr(III) at pH=4 in supernatant solution was measured (see methods part). As shown in Fig. S4, adsorbed Cr(VI) amount was 26.95 mg/g (31% of the total Cr(VI) removal) and reduced Cr(VI) amount was 62.13 mg/g (69% of the total Cr(VI) removal) after calculation, which indicated that most of the removed Cr(VI) was reduced to Cr(III). The fact illustrated that nZVI/BC actively participated in the removal of Cr(VI). It can be concluded that the enhanced removal of Cr(VI) is due to the multilayer structure of nZVI/BC/CA that facilitates the concurrent micro-electrolysis and adsorption of Cr(VI).

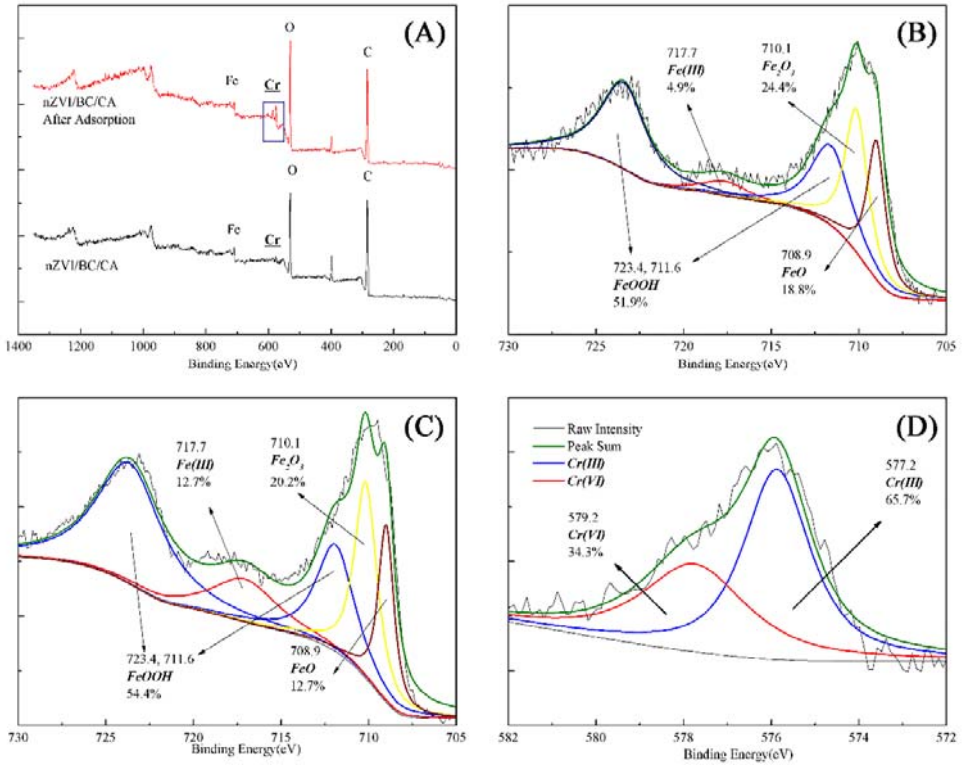

Fig. 5. XPS spectra of nZVI/BC/CA before and after adsorption [Initial Cr(VI) concentration = 150 mg/L, contact time = 24 h, temperature = 25°C, pH=4]: (a) full-scan survey; (b) Fe species; (c) Fe species after adsorption; and (d) adsorbed Cr species.

As depicted in Fig. 6, the removal pathways by nZVI/BC/CA could be divided into two parts, namely the outer layer and the inner structure. By the results of EDS and XPS analysis, the main component of the outer layer was CA and the role of outer layer was to: 1. Fulfill initial adsorption of Cr(VI) via ion exchange and hydrogen bonding of CA; 2. Transfer absorbed Cr(VI) to inner structure via intraparticle diffusion (micropores and crevices). Most of the nZVI/BC particles was entrapped by CA in the inner structure and the reduction of Cr(VI) happened within. The role of inner structure was: 1. Pre-adsorption of Cr(VI) via functional groups interactions (e.g. complexation, hydrogen boding, etc.) of CA and BC; 2. Micro-electrolysis between nZVI or Fe^{2+} (anode) and Cr(VI) (cathode) and the transfer of electrons through BC and CA, which enhanced the efficiency of redox reaction between reduced Fe species (nZVI or Fe^{2+}) and Cr(VI); 3. Post-adsorption of Cr(III) and residual Cr(VI) via CA and BC in deep micropores.

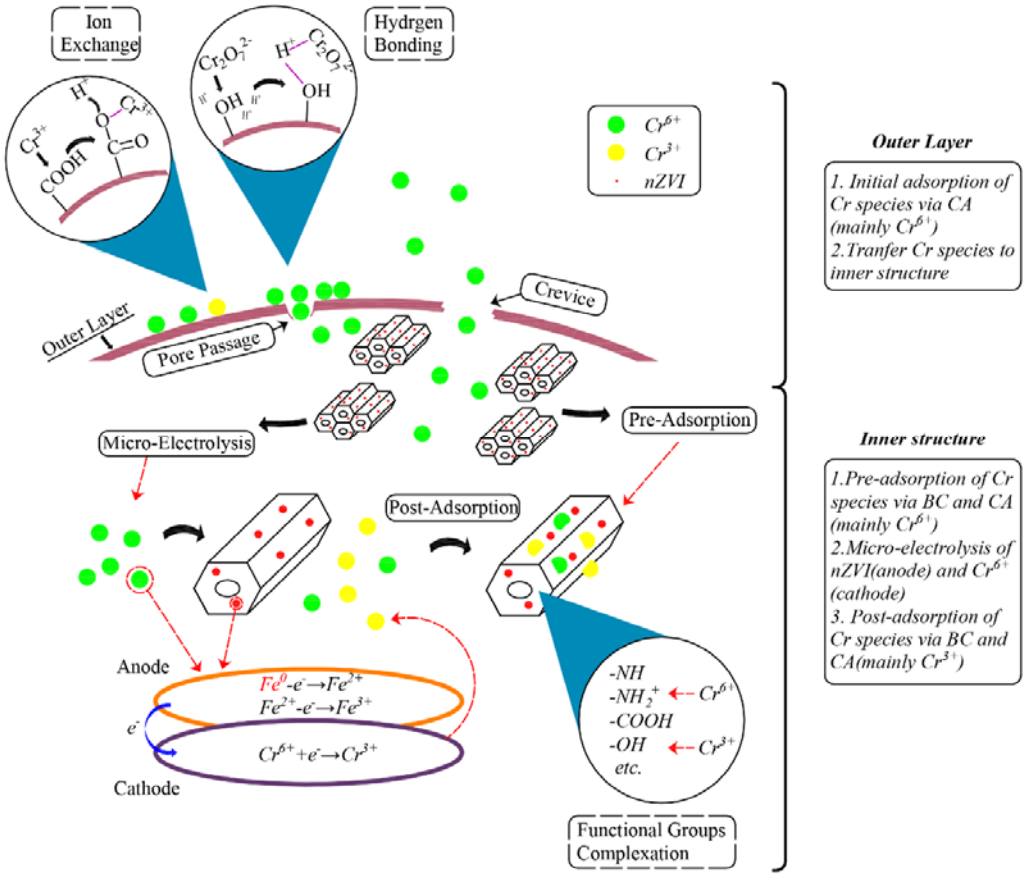

Fig. 6. Schematic diagram of concurrent micro-electrolysis and adsorption pathways.

The potential reactions in acidic solution were listed as follows:

Anode oxidation (Fe species):

$$Fe^0 - 2e^- \rightarrow Fe^{2+}, E^\theta(Fe^{2+}/Fe^0) \approx -0.44 \quad (9)$$

$$Fe^{2+} - e^- \rightarrow Fe^{3+}, E^\theta(Fe^{3+}/Fe^{2+}) \approx 0.77 \quad (10)$$

Cathode reduction (Cr^{6+}):

$$Cr_2O_7^{2-} + 14H^+ + 6e^- \rightarrow 2Cr^{3+} + 7H_2O, E^\theta(Cr^{6+}/Cr^{3+}) \approx 1.33 \quad (11)$$

In the micro-electrolysis system, Fe species (mainly Fe^0) acting as anode supplied electrons and BC or CA acting as cathode accelerated the redox reaction by accepting and transferring electrons to Cr(VI) without the need of direct contact between Fe^0 and Cr(VI). Thus, the generated Fe^{2+} could be retained in the deep structure with more retention time, which

426 created more reacting chance as Fe^{2+} anode resulting in a better removal performance and more
427 precipitation of iron oxides. In addition, the passivation of nZVI could be mitigated by reducing
428 the direct contact among reactants and nZVI with BC or CA acting as the electron shuttles.

429 3.4 Fixed-bed column evaluation

430 Fixed-bed column experiments were carried out to further investigate the practical
431 application of nZVI/BC/CA. In order to get a better understanding of the performance of
432 nZVI/BC/CA in fixed-bed column experiments, Thomas model was applied to analyze the
433 breakthrough curves and the results were listed in Table S6. As shown in Fig. 7 and Table S6,
434 faster saturation was reached and Thomas constant (k_{TH}) as well as maximal adsorption
435 capacity (q_m) increased with the rise of initial Cr(VI) concentration (C_0), which resulted from
436 the driving force and mass transfer flux from constant contact with influent Cr(VI). Thomas
437 model fitted the fixed-bed column experiments data well with the R^2 values more than 0.99,
438 suggesting nZVI/BC/CA could be suitable for the practical utilization. As shown in Fig. 7, The
439 concentration level decreased gradually below 1 mg/L as the retention time reached 1,800 min
440 at the initial Cr(VI) concentration of 150 mg/L, which concurred with conclusion in section
441 3.2. Recycling experiments were further carried out, in which 1 M NaOH was applied as the
442 eluent to remove adsorbed Cr species. The Cr(VI) removal capacity declined after the first
443 regeneration due to the consumption of nZVI in the composite. Yet the Cr(VI) removal capacity
444 remained stable during subsequent regeneration, suggesting that the utilized nZVI/BC/CA still
445 possessed the adsorption capacity of approximately 20 mg/g (Fig. S5). Thus, nZVI/BC/CA
446 possessed good prospect as potential low-cost and high-efficiency engineered biochar

composites for Cr removal from acidic wastewater.

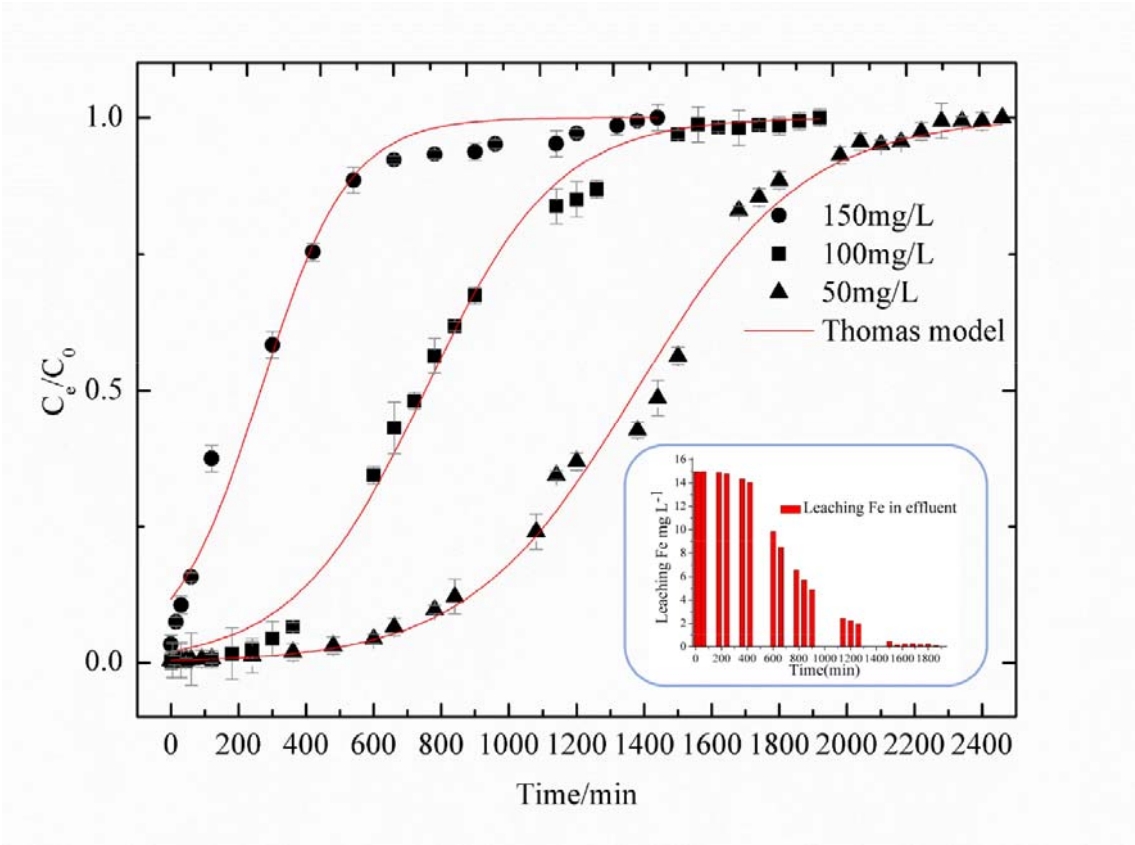

Fig. 7. Fixed-bed column experiments and leaching Fe amount in effluent (contact time = 24 h, temperature = 25°C, pH=4).

4. Conclusions

This study investigated the feasibility of entrapping nZVI impregnated biochar into Ca-alginate beads (nZVI/BC/CA) to increase the removal of Cr(VI) and reduce the side effect of the Fe leaching into the aqueous environment. The optimal pH for Cr(VI) removal was found to be 4 and the maximum Cr(VI) adsorption capacity estimated by Langmuir isotherm modeling was 86.43 mg/g for nZVI/BC/CA, larger than the simple combination of nZVI/BC and CA adsorption capacity. The mechanism of Cr(VI) reduction by nZVI/BC/CA composite

was mainly related to the multilayer structure and concurrent micro-electrolysis and adsorption . The nZVI/BC/CA could also be applied in fixed-bed column experiments, illustrating the feasibility of practical application of new engineered biochar composites.

5. Acknowledgement

This work was financially supported by the National Natural Science Foundation of China (51208397), Fundamental Research Funds for the Central Universities (2017II29GX), Key Technology R&D Program of Hubei Province (2015BCA304), and Hong Kong Research Grants Council (PolyU 15222115 and 15217818) for this study. The authors also appreciate the assistance offered by Tongji University.

6. References

Ahmad, M., Lee, S.S., Lee, S.E., Al-Wabel, M.I., Tsang, D.C.W., Ok, Y.S., 2017. Biochar-induced changes in soil properties affected immobilization/mobilization of metals/metalloids in contaminated soils. J Soil Sediment 17(3), 717-730.

Ahmed, M.B., Zhou, J.L., Ngo, H.H., Guo, W., Chen, M., 2016. Progress in the preparation and application of modified biochar for improved contaminant removal from water and wastewater. Bioresource technology 214, 836-851.

Ahmed, M.B., Zhou, J.L., Ngo, H.H., Guo, W.S., Johir, M.A.H., Sornalingam, K., Belhaj, D., Kallel, M., 2017. Nano-Fe-0 immobilized onto functionalized biochar gaining excellent stability during sorption and reduction of chloramphenicol via transforming to reusable magnetic composite. Chem Eng J 322, 571-581.

Banerjee, S., Joshi, S.R., Mandal, T., Halder, G., 2018. Application of zirconium caged activated biochar alginate beads towards deionization of Cr(VI) laden water in a fixed bed column reactor. J Environ Chem Eng 6, 4018-4029.

Beiyuan, J., Awad, Y.M., Beckers, F., Tsang, D.C.W., Ok, Y.S., Rinklebe, J., 2017. Mobility and phytoavailability of As and Pb in a contaminated soil using pine sawdust biochar under systematic change of redox conditions. Chemosphere 178, 110-118.

Chen, G.Q., Zhang, W.J., Zeng, G.M., Huang, J.H., Wang, L.A., Shen, G.L., 2011. Surface-modified Phanerochaete chrysosporium as a biosorbent for Cr(VI)-contaminated wastewater. Journal of Hazardous Materials 186(2-3), 2138-2143.

Cheng, Y.J., Yan, F.B., Huang, F., Chu, W.S., Pan, D.M., Chen, Z., Zheng, J.S., Yu, M.J., Lin, Z., Wu, Z.Y., 2010. Bioremediation of Cr(VI) and Immobilization as Cr(III) by Ochrobactrum anthropi. Environmental Science & Technology 44(16), 6357-6363.

Cho, D.W., Kwon, G., Yoon, K., Tsang, Y.F., Ok, Y.S., Kwon, E.E., Song, H., 2017a. Simultaneous production of syngas and magnetic biochar via pyrolysis of paper mill sludge using CO2 as reaction medium. Energ Convers Manage 145, 1-9.

Cho, D.W., Yoon, K., Kwon, E.E., Biswas, J.K., Song, H., 2017b. Fabrication of magnetic biochar 'as a treatment medium for As(V) via pyrolysis of FeCl3-pretreated spent coffee ground. Environ Pollut 229, 942-949.

Dong, H.R., Deng, J.M., Xie, Y.K., Zhang, C., Jiang, Z., Cheng, Y.J., Hou, K.J., Zeng, G.M., 2017a. Stabilization of nanoscale zero-valent iron (nZVI) with modified biochar for Cr(VI) removal from aqueous solution. Journal of Hazardous Materials 332, 79-86.

Dong, H.R., Zhao, F., He, Q., Xie, Y.K., Zeng, Y.L., Zhang, L.H., Tang, L., Zeng, G.M., 2017b. Physicochemical transformation of carboxymethyl cellulose-coated zero-valent iron nanoparticles (nZVI) in simulated groundwater under anaerobic conditions. Sep Purif Technol 175, 376-383.

Fang, S.E., Tsang, D.C.W., Zhou, F.S., Zhang, W.H., Qiu, R.L., 2016. Stabilization of cationic and anionic metal species in contaminated soils using sludge-derived biochar. Chemosphere 149, 263-271.

Feng, M., Zhang, W., Wu, X., Jia, Y., Jiang, C., Wei, H., Qiu, R., Tsang, D.C.W., 2018. Continuous leaching modifies the surface properties and metal(loid) sorption behaviour of sludge derived biochar. Sci. Total Environ. 625, 731-737.

Foo, K.Y., Hameed, B.H., 2010. Insights into the modeling of adsorption isotherm systems. Chem Eng J 156(1), 2-10.

Jobby, R., Jha, P., Yadav, A.K., Desai, N., 2018. Biosorption and biotransformation of hexavalent chromium [Cr(VI)]: A comprehensive review. Chemosphere 207, 255-266.

Jung, W., Jeon, B.H., Cho, D.W., Roh, H.S., Cho, Y., Kim, S.J., Lee, D.S., 2015. Sorptive removal of heavy metals with nano-sized carbon immobilized alginate beads. J Ind Eng Chem 26, 364-369.

Lecca, P., 2013. Stochastic chemical kinetics: A review of the modelling and simulation approaches. Biophysical Reviews 5, 323-345.

Lei, C., Sun, Y.Q., Khan, E., Chen, S.S., Tsang, D.C.W., Graham, N.J.D., Ok, Y.S., Yang, X., Lin, D.H., Feng, Y.J., Li, X.D., 2018a. Removal of chlorinated organic solvents from hydraulic fracturing wastewater by bare and entrapped nanoscale zero-valent iron. Chemosphere 196, 9-17.

Lei, C., Sun, Y.Q., Tsang, D.C.W., Lin, D.H., 2018b. Environmental transformations and ecological effects of iron-based nanoparticles. Environ Pollut 232, 10-30.

Li, H.D., Li, Z., Liu, T., Xiao, X., Peng, Z.H., Deng, L., 2008. A novel technology for biosorption and recovery hexavalent chromium in wastewater by bio-functional magnetic beads. Bioresource Technol 99(14), 6271-6279.

Li, Z.Z., Katsumi, T., Inui, T., Imaizumi, S., 2010. Woods Charred at Low Temperatures and Their Modification for the Adsorption of Cr(VI) Ions from Aqueous Solution. Adsorpt Sci Technol 28(5), 419-435.

Liu, T.Z., Tsang, D.C.W., Lo, I.M.C., 2008. Chromium(VI) reduction kinetics by zero-valent

iron in moderately hard water with humic acid: Iron dissolution and humic acid adsorption. Environmental Science & Technology 42(6), 2092-2098.

Lv, Z., Yang, S., Chen, L., Alsaedi, A., Hayat, T., Chen, C., 2018. Nanoscale zero-valent iron/magnetite carbon composites for highly efficient immobilization of U(VI). Journal of Environmental Sciences https://doi.org/10.1016/j.jes.2018.06.001.

Lyu, H.H., Tang, J.C., Huang, Y., Gai, L.S., Zeng, E.Y., Liber, K., Gong, Y.Y., 2017. Removal of hexavalent chromium from aqueous solutions by a novel biochar supported nanoscale iron sulfide composite. Chem Eng J 322, 516-524.

Ma, Y., Liu, W.J., Zhang, N., Li, Y.S., Jiang, H., Sheng, G.P., 2014. Polyethylenimine modified biochar adsorbent for hexavalent chromium removal from the aqueous solution. Bioresource Technol 169, 403-408.

Mortazavian, S., An, H., Chun, D., Moon, J., 2018. Activated carbon impregnated by zero-valent iron nanoparticles (AC/nZVI) optimized for simultaneous adsorption and reduction of aqueous hexavalent chromium: Material characterizations and kinetic studies. Chem Eng J 353, 781-795.

Peng, H., Gao, P., Chu, G., Pan, B., Peng, J., Xing, B., 2017. Enhanced adsorption of Cu(II) and Cd(II) by phosphoric acid-modified biochars. Environ Pollut 229, 846-853.

Periyasamy, S., Gopalakannan, V., Viswanathan, N., 2018. Hydrothermal assisted magnetic nano-hydroxyapatite encapsulated alginate beads for efficient Cr(VI) uptake from water. Journal of Environmental Chemical Engineering 6(1), 1443-1454.

Rajapaksha, A.U., Alam, M.S., Chen, N., Alessi, D.S., Igalavithana, A.D., Tsang, D.C.W., Ok, Y.S., 2018. Removal of hexavalent chromium in aqueous solutions using biochar: Chemical and spectroscopic investigations. Sci Total Environ 625, 1567-1573.

Ren, L., Dong, J., Chi, Z., Huang, H., 2018. Reduced graphene oxide-nano zero value iron (rGO-nZVI) micro-electrolysis accelerating Cr(VI) removal in aquifer. Journal of Environmental Sciences https://doi.org/10.1016/j.jes.2018.01.018.

Sazakli, E., Villanueva, C.M., Kogevinas, M., Maltezis, K., Mouzaki, A., Leotsinidis, M., 2014. Chromium in Drinking Water: Association with Biomarkers of Exposure and Effect. Int J Env Res Pub He 11(10), 10125-10145.

Shevchenko, N., Zaitsev, V., Walcarius, A., 2008. Bifunctionalized mesoporous silicas for Cr(VI) reduction and concomitant Cr(III) immobilization. Environmental Science & Technology 42(18), 6922-6928.

Sun, Y.Q., Lei, C., Khan, E., Chen, S.S., Tsang, D.C.W., Ok, Y.S., Lin, D.H., Feng, Y.J., Li, X.D., 2017. Nanoscale zero-valent iron for metal/metalloid removal from model hydraulic fracturing wastewater. Chemosphere 176, 315-323.

Sun, Y.Q., Lei, C., Khan, E., Chen, S.S., Tsang, D.C.W., Ok, Y.S., Lin, D.H., Feng, Y.J., Li, X.D., 2018. Aging effects on chemical transformation and metal(loid) removal by entrapped nanoscale zero-valent iron for hydraulic fracturing wastewater treatment. Sci Total Environ 615, 498-507.

Vikrant, K., Kim, K.H., Ok, Y.S., Tsang, D.C.W., Tsang, Y.F., Giri, B.S., Singh, R.S., 2018. Engineered/designer biochar for the removal of phosphate in water and wastewater. Sci Total Environ 616, 1242-1260.

Volesky, B., 2007. Biosorption and me. Water Research 41(18), 4017-4029.

Wan, Z.H., Li, M., Zhang, Q., Fan, Z.X., Verpoort, F., 2018. Concurrent reduction-adsorption

of chromium using m-phenylenediamine-modified magnetic chitosan: kinetics, isotherm, and mechanism. Environ Sci Pollut R 25(18), 17830-17841.

Wang, B., Gao, B., Wan, Y.S., 2018. Entrapment of ball-milled biochar in Ca-alginate beads for the removal of aqueous Cd(II). J Ind Eng Chem 61, 161-168.

Wang, T., Zhang, L.Y., Li, C.F., Yang, W.C., Song, T.T., Tang, C.J., Meng, Y., Dai, S., Wang, H.Y., Chai, L.Y., Luo, J., 2015. Synthesis of Core-Shell Magnetic Fe3O4@poly(m-Phenylenediamine) Particles for Chromium Reduction and Adsorption. Environmental Science & Technology 49(9), 5654-5662.

Wu, Y., Yue, Q., Ren, Z., Gao, B., 2018. Immobilization of nanoscale zero-valent iron particles (nZVI) with synthesized activated carbon for the adsorption and degradation of Chloramphenicol (CAP). Journal of Molecular Liquids 262, 19-28.

Yang, F., Zhang, S., Sun, Y., Cheng, K., Li, J., Tsang, D.C.W., 2018. Fabrication and characterization of hydrophilic corn stalk biochar-supported nanoscale zero-valent iron composites for efficient metal removal. Bioresource Technol 265, 490-497.

Yen, M.Y., Teng, C.C., Hsiao, M.C., Liu, P.I., Chuang, W.P., Ma, C.C.M., Hsieh, C.K., Tsai, M.C., Tsai, C.H., 2011. Platinum nanoparticles/graphene composite catalyst as a novel composite counter electrode for high performance dye-sensitized solar cells. Journal of Materials Chemistry 21(34), 12880-12888.

Zhong, D., Zhang, Y., Wang, L., Chen, J., Jiang, Y., Tsang, D.C.W., Zhao, Z., Ren, S., Liu, Z., Crittenden, J.C., 2018. Mechanistic insights into adsorption and reduction of hexavalent chromium from water using magnetic biochar composites: Key roles of Fe3O4 and persistent free radicals. Environ. Pollut. in press.

Zhu, S., Huang, X., Ma, F., Wang, L., Duan, X., Wang, S., 2018. Catalytic Removal of Aqueous Contaminants on N-Doped Graphitic Biochars: Inherent Roles of Adsorption and Nonradical Mechanisms. Environmental science & technology 52(15), 8649-8658.